

Photo-induced CO₂ cycloaddition and tetracycline degradation over novel FeO_x modified defective graphitic carbon nitride composite

Ruolin Cheng ^a, Jing Ren ^b, Haoran Wang ^b, Huagen Liang ^{a,c,d,*}, Panagiotis Tsakaratas ^{d,**}

^a Jiangsu Key Laboratory of Coal-based Greenhouse Gas Control and Utilization, Carbon Neutrality Institute, China University of Mining and Technology, Xuzhou, Jiangsu 221008, China

^b School of Information and Control Engineering, China University of Mining and Technology, Xuzhou 221116, China

^c School of Materials Science and Physics, China University of Mining and Technology, Xuzhou 221008, China

^d Laboratory of Alternative Energy Conversion Systems, Department of Mechanical Engineering, School of Engineering, University of Thessaly, Pedion Areos 38834, Greece



ARTICLE INFO

Keywords:

g-C₃N₄
Defect engineering
Photocatalytic CO₂ cycloaddition
Tetracycline degradation

ABSTRACT

Utilizing sunlight to achieve CO₂ conversion and environmental remediation has been a key focus. Herein, “all-in-one” graphitic carbon nitride (g-C₃N₄) composite-based photocatalysts were synthesized by a simple one-step low-temperature calcination. Lower calcination temperature resulted in defective g-C₃N₄ enriched in cyano and hydroxyl groups. It was found that by incorporating amorphous FeO_x, the resulted FeO_x/O-g-C₃N₄ photocatalyst shows very good performance towards both CO₂ cycloaddition reaction and photo-Fenton degradation of tetracycline (TC). It was also found that the photocatalyst shows the highest styrene carbonate yield of 83% (23 mmol g⁻¹ h⁻¹) under ambient conditions, which is 13.8 times higher than that obtained over pure g-C₃N₄. The photocatalyst also exhibits a 4.7 times faster TC removal rate than that of pure g-C₃N₄. Systematic characterization and mechanism study demonstrate the role of defects and photo-induced charge carriers.

1. Introduction

The environmental crisis of global warming related to the rapid increase in atmospheric CO₂ concentration, and soil and water pollution caused by the extensive use of antibiotics call for immediate measures [1,2]. The coupling of CO₂ and epoxides is an appealing CO₂ conversion strategy, where the cyclic carbonates produced are widely used as intermediates in fine chemical synthesis and electrolytes for lithium-ion batteries [3]. Cause the ring-opening of epoxides is generally considered to be the rate-determining step of CO₂ cycloaddition reaction, most studies focus on constructing catalysts rich in Lewis acidic sites to promote the activation of epoxides [4]. Hydrogen bonding donor (HBD) groups, including hydroxyl (-OH), amino (-NH₂), and carboxyl (-COOH) have also been reported to activate epoxides through hydrogen bonding, thereby enhancing the performance of CO₂ cycloaddition reactions [5]. Nevertheless, this reaction is still mostly carried out under high temperature and pressure for a long reaction time.

Graphite carbon nitride (g-C₃N₄) is known for its excellent electronic

properties, rich in nitrogen-containing groups, and unique band gap structure, exhibiting great potential in CO₂ cycloaddition reaction and organic pollutant degradation [6–12]. However, cause g-C₃N₄ is commonly synthesized by high-temperature calcination at around 550 °C, its specific surface area is low, and charge transfer is inhibited. Thus, pure g-C₃N₄ has been coupled with other materials for satisfactory antibiotics removal efficiency [13]. Moreover, due to the intrinsic scarcity of Lewis acid sites, pure g-C₃N₄ can hardly activate epoxides. Cocatalysts loading is a commonly used method for the photoactivity improvement of g-C₃N₄, but the reaction still needs to be conducted under 90–140 °C and 1.5–2 MPa [14–17]. Recently, there have been studies on g-C₃N₄-based photocatalysts, which utilize photoelectrons and holes to initiate CO₂ cycloaddition reaction under mild conditions. However, the reaction systems suffer from low carbonate yields and complex catalyst synthesis [18,19].

In this work, we synthesized amorphous iron oxide (FeO_x) modified defective g-C₃N₄ by a one-step low-temperature calcination method. Cyano (-C≡N) and hydroxyl (-OH) groups were introduced into

* Corresponding author at: Jiangsu Key Laboratory of Coal-based Greenhouse Gas Control and Utilization, Carbon Neutrality Institute, China University of Mining and Technology, Xuzhou, Jiangsu 221008, China

** Corresponding author.

E-mail addresses: lianghg@cumt.edu.cn (H. Liang), tsik@uth.gr (P. Tsakaratas).

defective g-C₃N₄ without acid/alkali corrosion or secondary calcination. Combined with the Lewis acidic oxide FeO_X, the catalysts contain abundant Lewis acidic sites and HBD groups, greatly enhancing its performance in photocatalytic CO₂ cycloaddition. Furthermore, the amorphous FeO_X species anchored on g-C₃N₄ is composed of higher proportion of Fe²⁺ than Fe³⁺, which is conducive to the Photo-Fenton tetracycline removal. We report for the first time the construction of “all-in-one” dual-functional g-C₃N₄-based photocatalysts with superb photoactivity for CO₂ cycloaddition and tetracycline degradation. The mechanisms of both reactions are discussed.

2. Experimental section

2.1. Chemicals and reagents

Urea (98%), ferrocene (99%), tetrabutyl ammonium bromide (TBAB, 99%), styrene oxide (98%), dodecane (98%), ferric oxide (Fe₂O₃, ≥99%), ferroferric oxide (Fe₃O₄, 99%), ferric nitrate nonahydrate (Fe (NO₃)₃•9 H₂O, 99.9%), N,N-dimethylformamide (DMF, 99.5%), sodium sulfate (Na₂SO₄, 99%), hydrogen peroxide solution (H₂O₂, 30%), potassium persulfate (K₂S₂O₈, 99.5%), and methanol (MeOH, 99.5%), isopropyl alcohol (IPA, ≥99.7%), p-benzoquinone (BQ, 99%), disodium ethylenediamine-tetraacetate (EDTA-2Na), L-histidine (≥99%) were from Shanghai Aladdin Biochemical Science and Technology Co. Ltd. and used directly.

2.2. Synthesis of FeO_X modified oxygen-enriched g-C₃N₄

A low-temperature one-step calcination approach was applied: 4 g urea and controlled amount of ferrocene were physically mixed and calcined for 1 h at 405 °C with a ramp of 5 °C min⁻¹. The obtained FeO_X/O-g-C₃N₄ samples were denoted as CNOFe-Xs, where X stands for the quantity of ferrocene added (X=1, 2, 3 g). The sample synthesized without ferrocene added was denoted as MCA.

2.3. Synthesis of FeO_X modified g-C₃N₄

The g-C₃N₄ (CN) and FeO_X/g-C₃N₄ (CNFe-Xs) samples were synthesized by calcinating a physical mixture of 10 g urea and a suitable quantity of ferrocene (X=0, 1, 2, 3 g) at 500 °C with a ramp of 5 °C min⁻¹ for 2 h.

2.4. Characterization

X-ray diffractometry (XRD) data were acquired on a Bruker D8 Advance diffractometer. Inductive Coupled Plasma Emission Spectrometer (ICP-OES) results were obtained on a Thermo ICAP PRO. Fourier transform infrared (FTIR) signals were scanned on a Nicolet iS 10. The morphology and elemental distribution of the samples were examined using a JEM2100F transmission electron microscope (TEM) and an FEI-Q FEG250 scanning electron microscope (SEM). Al K α was used as the excitation source for the X-ray photoelectron spectroscopy (XPS) measurement on a Thermo ESCALAB 250Xi spectrometer. In-situ XPS was measured on a PHI 5000 Versaprobe III. The light response of the samples was acquired from a Shimadzu UV2600 spectrophotometer. An Edinburgh FLS1000 was used to record the steady-state photoluminescence (PL) spectra under an excitation wavelength of 380 nm and time-resolved fluorescence (TRPL) decay curves using a 375 nm laser as the excitation source. N₂ and CO₂ gas adsorption analyses were conducted on a Quantachrome Autosorb-iQ at 77 K and 273 K, respectively. Temperature programmed desorption of ammonia (NH₃-TPD) analysis was conducted on Micromeritics AutoChem II 2920. Electron paramagnetic resonance (EPR) spectra were recorded on a Bruker EMXplus.

2.5. Photocatalytic CO₂ cycloaddition of styrene oxide

Styrene oxide was used as the target substrate to characterize the photocatalytic properties of the resulting materials. The experimental procedure was as follows: 30 mg of catalyst and 36 mg of TBAB were added to 10 mL DMF solution of styrene oxide (concentration of 1 mol L⁻¹). The reaction was performed in an environment of 1 bar CO₂ and ambient temperature, using a 300 W xenon lamp equipped with an air mass (AM) 1.5 filter as the light source. After 12 h irradiation, the solution was centrifuged and extracted with a 1:1 vol ratio of ethyl acetate and deionized water. Using dodecane as the internal standard, gas chromatography (GC) measurement was performed on Fuli GC-9790 equipped with an FID detector and DB-17 column. In the cyclic stability test, four consecutive reactions (every 12 h) were performed. The reaction temperature variations were measured by a Testo 869 infrared camera.

The catalysts' performance was assessed by the yield and selectivity of styrene carbonate. Yield (%): $X = C_{SC}/C_0 \times 100$, yield (mmol g⁻¹ h⁻¹): $Y = N_{SC}/(W \times t)$, and selectivity (%): $S = C_{SC}/(C_0 - C_{SO}) \times 100$, where C₀, C_{SO}, and C_{SC} stand for the concentration of styrene oxide before and after the reaction, as well as the concentration of styrene carbonate produced, respectively. Moreover, N_{SC}, W, and t are the amount of styrene carbonate, the mass of catalysts, and the reaction time, respectively.

The apparent quantum efficiency (AQE) was measured with 350, 400, 450, 500, 550 and 600 nm band-pass filters, separately. The irradiation intensity was measured by a CEL-NP2000 spectroradiometer and the AQE was calculated as: AQE (%) = number of evolved styrene carbonate molecules × 100/number of incident photons.

2.6. Photo-Fenton removal of tetracycline (TC)

The samples' photo-Fenton degradation performance was evaluated by the removal rate of TC. 20 mg catalyst was added to 100 mL TC solution (20 mg L⁻¹) and the suspension was agitated in dark for 30 minutes to obtain a dynamic equilibrium of adsorption and desorption. Afterwards, 200 μL H₂O₂ was added to the suspension. Stimulated sunlight was created by a Xenon lamp with an AM1.5 filter. Every 10 minutes of illumination, 3 mL solution was extracted and filtered for UV-Vis analysis. The TC removal efficiency was calculated from the difference between residual TC concentration (C_t) and initial TC concentration (C₀). The TC removal rate was fitted by the first-order kinetic equation (-ln (C_t/C₀) = kt), where k (min⁻¹) stands for the rate constant, and t represents the reaction time.

2.7. Photoelectrochemical analysis

Photoelectrochemical measurements were conducted on a DH7000 electrochemical workstation using a typical three-electrode electrolytic cell with 0.2 mol L⁻¹ Na₂SO₄ solution as the electrolyte. Platinum was used as counter electrode and Ag/AgCl electrode was the reference. 20 mg catalyst was deposited on a fluorine-doped tin oxide (FTO) glass with a controlled deposition area of 1 cm² to obtain a working electrode. Electrochemical impedance spectroscopy (EIS) was performed in the dark at -0.4 V. The chopped photocurrent was measured at 0.4 V with respect to the reference electrode under irradiation. Mott-Schottky plots were measured at 1.0 kHz and 1.5 kHz in dark.

3. Results and discussion

3.1. Physicochemical characterizations

XRD was first performed to analyze the catalysts' microstructure. As can be seen from Fig. 1a the MCA obtained by calcination of urea at 405 °C has two main diffraction peaks ($2\theta = 10.8^\circ$ and 27.9°), matching well with the XRD pattern of intermediate melamine cyanurate.

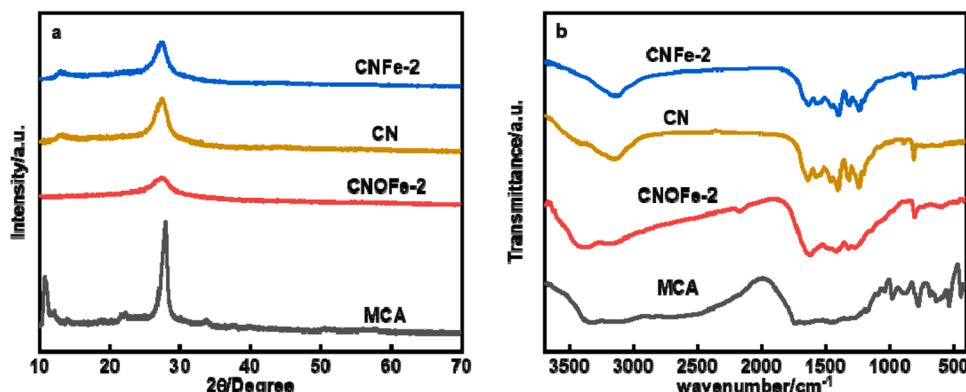


Fig. 1. (a) XRD and (b) FT-IR spectra of CNOFe-Xs and CNFe-Xs.

The addition of ferrocene promotes the completion of g-C₃N₄ structure, with the g-C₃N₄ (002) peak in the CNOFe-2 samples shifting to 27.3° [20]. It is noteworthy that compared with CN synthesized at 500 °C, the (100) peak is not obvious in CNOFe-2 and its (002) peak is slightly negatively shifted, indicating a less ordered tri-s-triazine in-plane stacking and relatively loose interlayer stacking. The pattern of CNFe-2 is consistent with CN. Also, the same behaviour can be observed in CNOFe-Xs (Figure S1a) and CNFe-Xs (Figure S1b) samples, where the (002) peak gradually broadens with the increase of ferrocene content, suggesting the decreased polymerization degree of g-C₃N₄'s interlayer network. In addition, no characteristic peaks from ferric species were observed in all samples, due to the trace amount of Fe inside (Table S1).

From the FT-IR results presented in Fig. 1b, it is further revealed that MCA (the sample without ferrocene) exhibits the same pattern as the intermediate melamine cyanurate, with peaks at 770 cm⁻¹ and 1735 cm⁻¹ from triazine and C=O, respectively. The CNOFe-2, CN, and CNFe-2 basically present the typical g-C₃N₄ structure. The peak at 810 cm⁻¹ is allocated to the bending mode of tri-s-triazine units. The broad peaks at 1200–1650 cm⁻¹ belong to the typical stretching vibration of aromatic C-N heterocycles. Remarkably, a strong peak at 2177 cm⁻¹ from the stretching mode of -C≡N can only be observed in CNOFe-2 [21]. Compared with CN and CNFe-2, CNOFe-2 exhibits significantly broaden peaks belonging to surface amino (-NH₂) and -OH groups at 3000–3600 cm⁻¹, which can be attributed to the stronger surface OH stretching (3340 cm⁻¹) [22]. Moreover, a peak at 565 cm⁻¹ attributed to the stretching vibration mode of Fe-O can be observed in CNOFe-2 and CNFe-2 (Figure S1c), indicating that the Fe species in the samples are present in the form of amorphous iron oxides (FeO_x) [23].

As displayed in Fig. 2a, clear C, N, O, and Fe signals were detected in the XPS full spectra of CNOFe-2 and CNFe-2. The surface atomic ratios of C, N, and O in CN and CNFe-2 are similar, but very different from that of CNOFe-2 (as listed in Table S2).

Peak splitting of Fe 2p, C 1s, N 1s, and O 1s was performed to analyze the catalysts' structure in more detail. The Fe 2p spectra of CNOFe-2 (Fig. 2b) and CNFe-2 (Fig. 2c) show doublets from Fe²⁺ (at 710.6 and 723.6 eV) and Fe³⁺ (at 712.3 and 725.3 eV) [24]. In agreement with literature report, the proportion of Fe²⁺ is calculated to be 52%, which is slightly higher than Fe³⁺ (48%) in the amorphous FeO_x [25].

The C1s spectra can be divided into three peaks located at 288.1, 286.3, and 284.8 eV, which correspond to the N-C≡N coordination in g-C₃N₄ heterocycle, C-NH₂, and adventitious carbon, respectively (Fig. 2d) [26]. Compared to CN and CNFe-2, the CNOFe-2 has a significantly increased peak at 286.3 eV. This is due to the fact that the -C≡N has a similar binding energy as C-NH₂, further confirming the existence of -C≡N groups in CNOFe-2, which is in consistence with the FTIR result [27]. As displayed in Fig. 2e, the N 1s spectra validate four peaks ascribed to sp² hybridized N (C-N=C) at 398.6 eV, sp³ hybridized N

(N-(C)3) at 399.9 eV, N-H groups at 401.0 eV, and π-electron excitation at 404.2 eV, respectively [28]. The intensity ratio of N_{sp2}/N_{sp3} dropped from 4.3 in CN to 3.5 in CNO-F2. CNOFe-2 also exhibits an obvious lower N/C ratio (1.09) than that of CN (1.27). It is suggested that -C≡N groups are formed through the broken of C-N=C bonds [27].

Moreover, the ratio of O in CNOFe-2 (7.52%) far exceeds that in CN (3.33%) and CNFe-2 (3.88%). As depicted in Fig. 2f, the oxygen species in CN are mainly adsorbed H₂O and oxygen with peaks at 531.9 and 533.3 eV, respectively [29]. In CNFe-2 and CNOFe-2, the peak belonging to O²⁻ in iron oxide can be observed at 530 eV [23]. Moreover, an obvious peak at 531.1 eV assigned to C-O-H groups appeared in CNOFe-2 [30].

Overall, the above data confirm the successful construction of FeO_x/O-g-C₃N₄ and FeO_x/g-C₃N₄ photocatalysts. CNFe-2 obtained from 500 °C calcination mainly maintains the same structure as g-C₃N₄. Lower calcination temperature (405 °C) endows CNOFe-2 with abundant -C≡N and -OH groups, which are beneficial for the capture and activation of CO₂ and epoxides.

Morphologically, high-temperature calcination results in block-like agglomerates of CN (Fig. 3a) and CNFe-2 (Fig. 3b), but the particle size of CNFe-2 significantly decreased. On the contrary, the CNOFe-2 sheets obtained from lower heating temperature are thinned and curled, forming a novel porous lamellar structure (Fig. 3c). The corresponding SEM elemental mappings of CNFe-2 (Figure S2) and CNOFe-2 (Figure S3) further confirm the well-dispersion of FeO_x on g-C₃N₄ and O-g-C₃N₄. According to the XRD and XPS analysis of CNOFe-2, no obvious lattice fringes are seen in the HRTEM image (Fig. 3d), as the oxygen-enriched g-C₃N₄ is not highly crystalline, and the iron oxide is in an amorphous form.

Consistently, all three samples show type IV N₂ adsorption-desorption isotherms with H3 hysteresis loop, ascribing to the narrow slit-shaped channels (Figure S4a). The specific surface area (S_{BET}) of the three samples, from low to high, are CN (43 m²g⁻¹), CNOFe-2 (59 m²g⁻¹), and CNFe-2 (76 m²g⁻¹), mainly due to the increase in the number of mesopores and macropores (Figure S4b). It is known that S_{BET}, light absorption capacity, and charge carrier separation efficiency of the photocatalysts play important roles in their performance. Fig. 4a shows that FeO_x modification improves the light absorption ability of the catalysts. Due to the low content of FeO_x in the catalysts, the PL spectra of CNFe-2 and CNOFe-2 only have one characteristic peak from g-C₃N₄ at around 460 nm, as shown in Fig. 4b. Compared to CN, an obvious decrease in PL intensity can be seen in CNFe-2 and CNOFe-2, suggesting that charge separation is promoted [28]. TRPL decay curves were further measured and fitted with a biexponential decay function (Figure S5). The fluorescence lifetime of FeO_x modified samples are significantly shortened compared to pure CN, indicating efficient transfer of photogenerated electrons from g-C₃N₄ to FeO_x, leading to fluorescence quenching [31].

Photoelectrochemical tests further confirm the improved charge

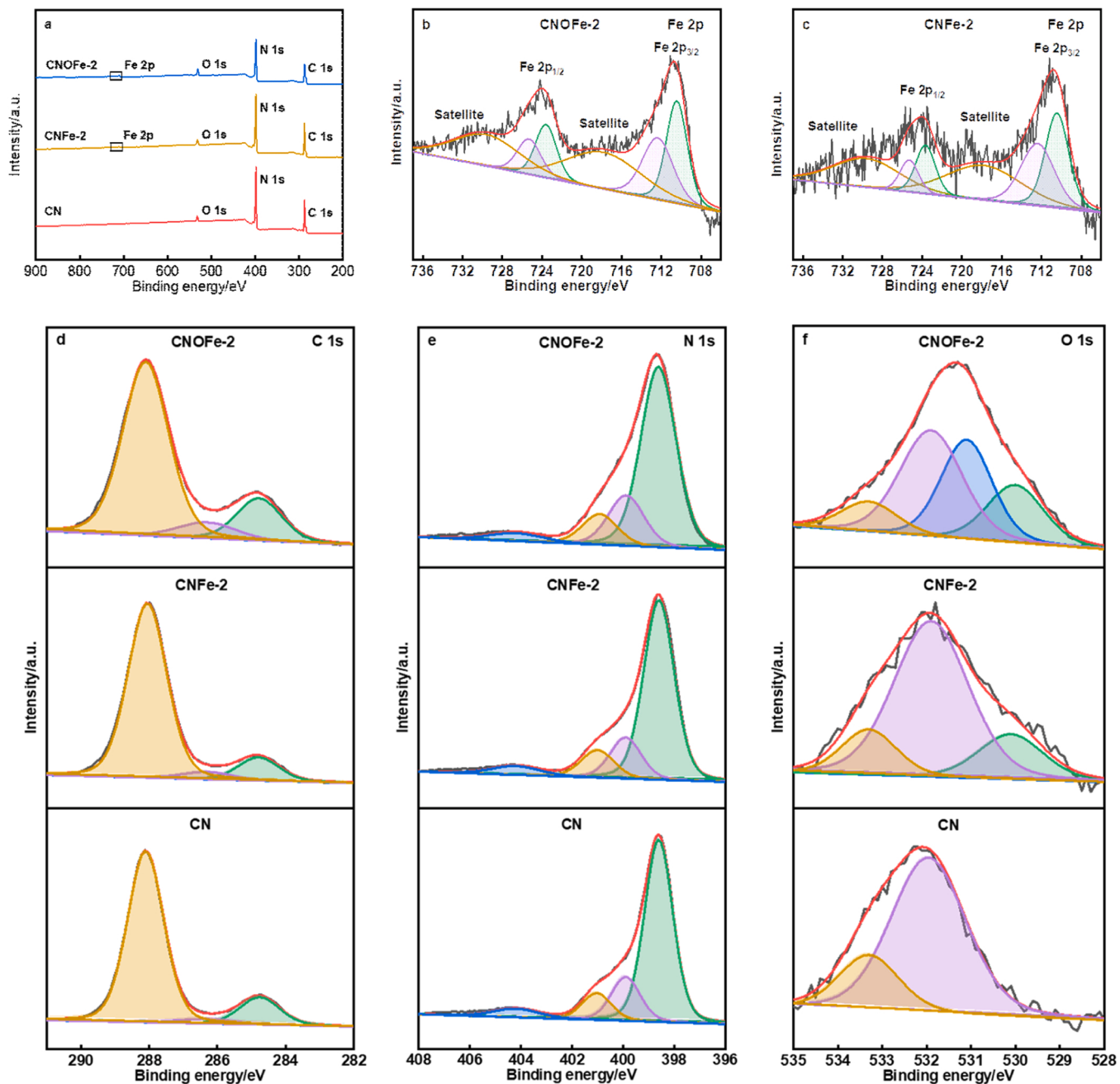


Fig. 2. XPS spectra of CN, CNFe-2, and CNOFe-2: (a) full spectra, (b-c) Fe 2p, (d) C 1 s, (e) N 1 s, and (f) O 1 s.

carrier transfer after FeO_x modification. Compared to that of CN and CNFe-2, CNOFe-2 shows the lowest dark impedance (Fig. 4c), while its photocurrent is the highest (Fig. 4d). Thus, the enhanced light-harvesting ability and photogenerated carriers transfer capacity of CNOFe-2 endows it with a significant increase in photoactivity.

3.2. Photocatalytic CO_2 cycloaddition of styrene oxide

All samples' photoactivity was evaluated by the coupling of CO_2 and styrene oxide without additional heating and pressure. As depicted in Figure S6a, all samples exhibit excellent styrene carbonate selectivity (> 99%). No product was detected under N_2 atmosphere or in dark. The blank test shows about 1% yield of styrene carbonate without any addition of catalyst. With FeO_x incorporation, CNOFe-Xs (Fig. 5a) and CNFe-Xs (Fig. 5b) exhibit dramatically improved photocatalytic performance.

In terms of activity, CNOFe-Xs (FeO_x modified oxygen-enriched g-C₃N₄) exhibit superior performance compared to CNFe-Xs (FeO_x modified g-C₃N₄). Notably, CNOFe-2 stands out with an exceptional 83% styrene carbonate yield after 12 hours of irradiation. This yield rate is 3.6 times higher than that of CNFe-2 and an impressive 13.8 times higher than CN. This underscores the heightened reactivity of CNOFe-2 in the given experimental conditions, suggesting its potential significance in the studied chemical reaction or process under irradiation. Figure S6b shows the temperature change of CNOFe-2 under irradiation, tracked by infrared thermography (Figure S6c). The temperature rapidly increased from 22.4 °C to 63.1 °C after 15 min irradiation and remained below 80 °C throughout the entire 12 h reaction. Therefore, a control test was carried out in dark at 80 °C, and the photoactivity of CNOFe-2 decreased dramatically (steep styrene carbonate yield decrease from 83% to 9%), highlighting the important role of photogenerated charge carriers in the reaction. CNOFe-2 shows good performance (Figure S7a)

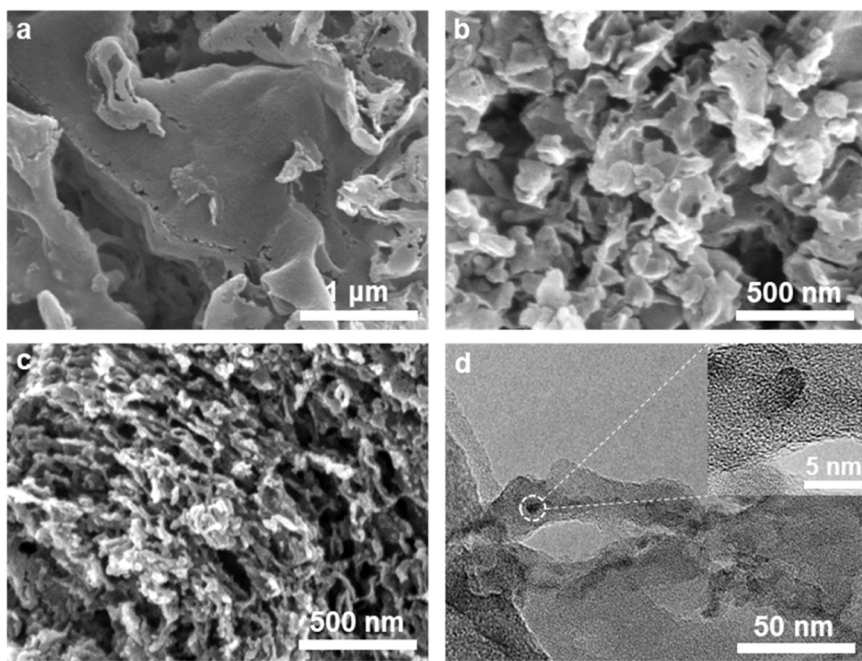


Fig. 3. Typical SEM images of: (a) CN, (b) CNFe-2, (c) CNOFe-2 and (d) TEM image of CNOFe-2.

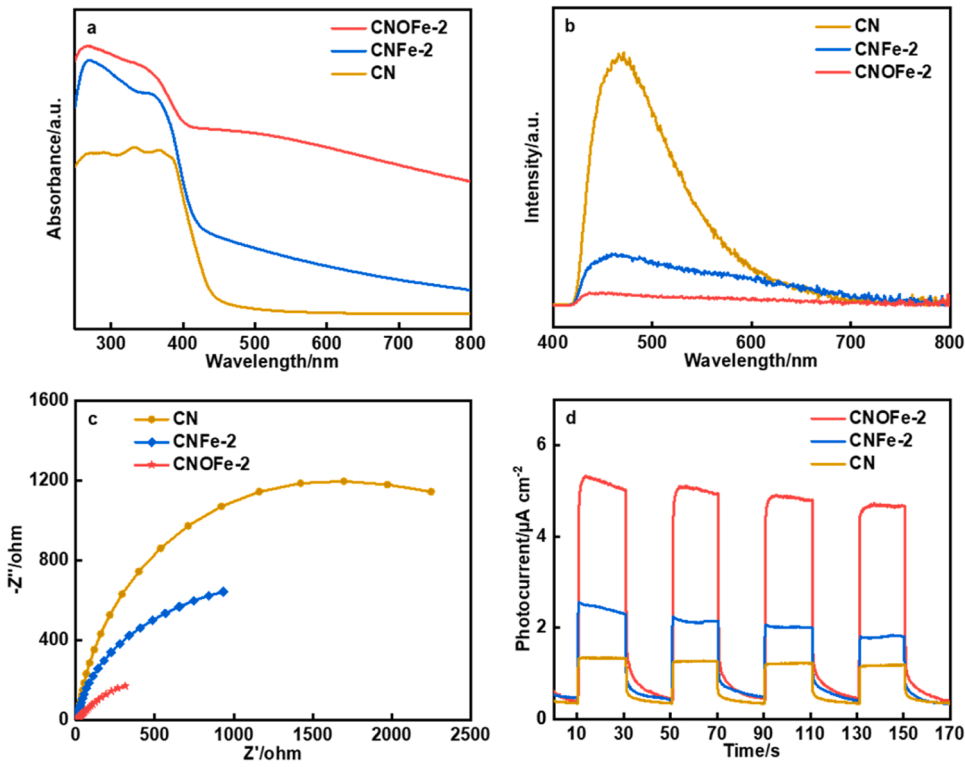


Fig. 4. (a) UV-vis absorption spectra, (b) PL spectra (excitation wavelength: 380 nm), (c) EIS Nyquist plots and (d) chopped photocurrent of the samples.

and structural stability (Figure S7(b-d)) in 4 consecutive reactions (12 h each). For comparison, pure Fe_2O_3 and Fe_3O_4 are not active. The Fe precursors were switched from ferrocene to Fe_2O_3 , Fe_3O_4 and $\text{Fe}(\text{NO}_3)_3 \bullet 9 \text{H}_2\text{O}$, and the resulting low-temperature calcinated samples showed very low styrene carbonate yield rate of 2%, 4% and 12%. Compared to reported catalytic systems (Table 1), $\text{FeO}_x/\text{O-g-C}_3\text{N}_4$ photocatalysts have an outstanding advantage in the styrene carbonate production under moderate condition, with a styrene carbonate yield of

$23 \text{ mmol g}^{-1}\text{h}^{-1}$. The apparent quantum efficiencies (AQE) of CNOFe-2 under different incident light wavelengths have been calculated and depicted in Figure S8. CNOFe-2 exhibited the highest AQE of 3.7% at 350 nm.

Considering that CO_2 adsorption capacity and Lewis acid sites are critical factors in CO_2 cycloaddition reaction, CO_2 adsorption analysis was first carried out. Fig. 5c reveals that CNFe-2 has a slightly higher CO_2 adsorption ability than CN, arising from increased S_{BET} . The CO_2

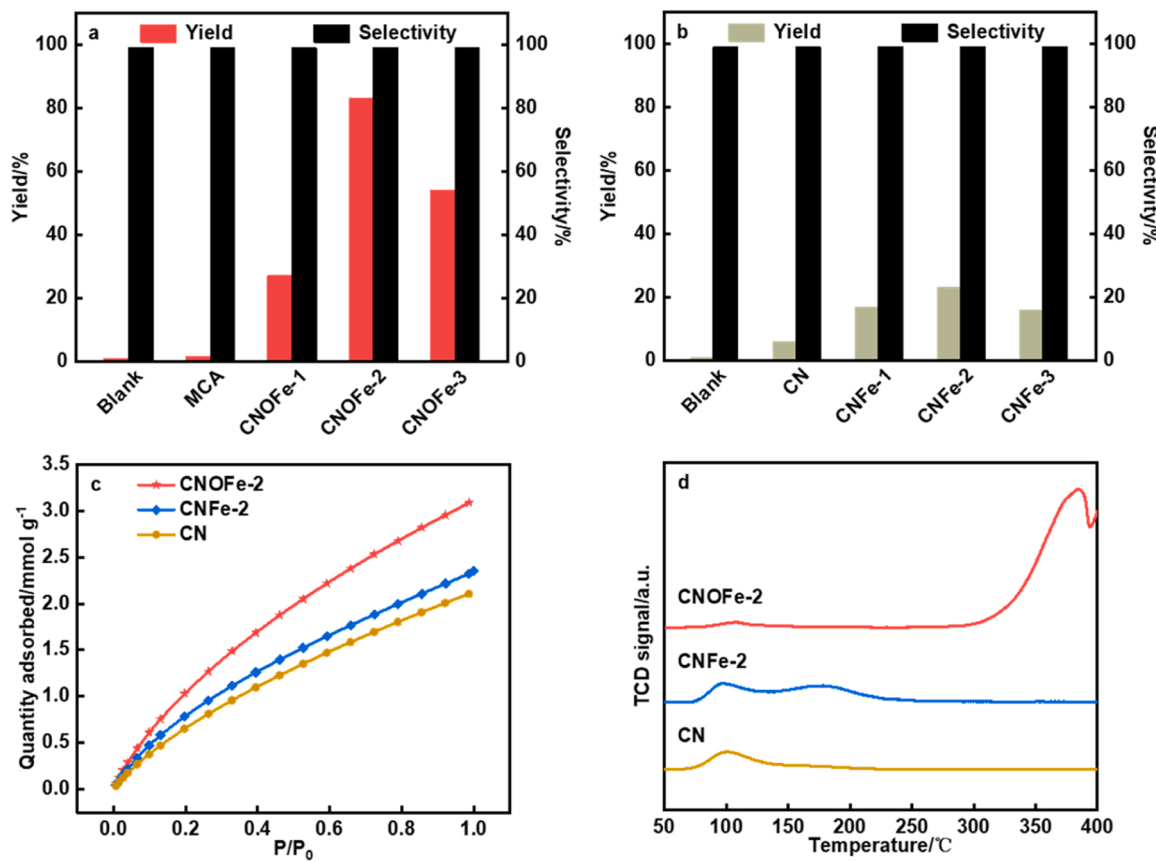


Fig. 5. Photocatalytic CO₂ cycloaddition performance of (a) CNOFe-Xs and (b) CNFe-Xs; (c) CO₂ adsorption isotherms and (d) NH₃-TPD profiles of the samples.

Table 1
Previously reported studies on styrene carbonate production.

Catalyst	Parameters	Time/h	Yield ^a /%	Yield ^b /mmol g ⁻¹ h ⁻¹	Ref
Pd/g-C ₃ N ₄	0.75 W/cm ² blue LED	24	97	0.6	[18]
Bi-PCN-224	300 W Xe lamp Full spectrum	6	98	6	[32]
Zn-Uio-67-bpydc	300 W Xe lamp Full spectrum	9	75	0.3	[33]
Fe-BTC	30 W blue LED	6	90	1	[34]
Ag/g-C ₃ N ₄	300 W Xe lamp Full spectrum	6	26	183	[35]
Co _{1-x} ZnIn ₂ S ₄	300 W Xe lamp $\lambda > 420$ nm	24	80	5	[36]
CdS/CeO ₂	300 W Xe lamp Full spectrum	24	96	0.4	[37]
FeOx/O-g-C ₃ N ₄	300 W Xe lamp Full spectrum	12	83	23	This work

^a Yield (%) = $C_{SC}/C_0 \times 100$, where C_0 and C_{SC} stand for the concentration of styrene oxide before the reaction, and the concentration of styrene carbonate produced, respectively.

^b Yield (mmol g⁻¹ h⁻¹) = $N_{SC}/(W \times t)$, where N_{SC} , W , and t represent the amount of styrene carbonate generated, the weight of the catalyst, and the reaction time, respectively.

adsorption ability of CNOFe-2 is further enhanced to 1.4 times higher than CN. Furthermore, NH₃-TPD tests were performed to evaluate the samples' acidity (Fig. 5d). CN only has one desorption peak from physically adsorbed NH₃ at 100 °C, corresponding to its intrinsic basicity. In addition to the physisorbed NH₃, CNFe-2 has an extra peak located at about 180 °C, arising from the weak Lewis acid sites. Differently, the dominant peak of CNOFe-2 is at about 380 °C, indicating the

presence of medium-strong acidic sites in the sample.

In order to gain a deeper understanding of the substrate adsorption, the adsorption energy of CO₂ and styrene oxide on the surface of g-C₃N₄ and O-g-C₃N₄ were evaluated by density functional theory (DFT). In the simulated structures (Figure S9), the adsorption energy of CO₂ on O-g-C₃N₄ is lower than that of g-C₃N₄. The presence of -OH groups make the adsorption energy of styrene oxide on O-g-C₃N₄ much lower than that of g-C₃N₄, which can be attributed to the establishment of hydrogen bonds between the -OH groups and styrene oxide [38]. Thus, O-g-C₃N₄ is more favorable for the adsorption of CO₂ and styrene oxide.

The role of photogenerated carriers was analyzed by EPR experiments using the principle that photogenerated electrons can reduce TEMPO (2, 2, 6, 6-tetramethylpiperidine-1-oxyl), leading to a decreased triple-peak intensity [39]. Light on for 5 minutes, the peak intensities in N₂ (Fig. 6a) and CO₂ (Fig. 6b) decreased to a similar extent of 22% and 14%, respectively, reflecting that photogenerated electrons can hardly transfer to CO₂. Notably, as illustrated in Fig. 6c, additional styrene oxide addition only led to 2% decrease in signal intensity, indicating that the photogenerated electrons on the catalyst would swiftly move to the epoxide. Moreover, quenching experiments were performed on CNOFe-2 to explore the role of photoelectrons and holes (Fig. 6d). K₂S₂O₈ was first used to capture photoelectrons and the styrene carbonate yield plunged from 83% to 14%. Subsequently, the styrene carbonate yield dropped to 63% after the addition of hole quencher MeOH. Thus, both photogenerated electrons and holes are significant contributors to the reaction, albeit the electrons are more so.

In-situ XPS analysis was conducted on CN and CNOFe-2 before and after irradiation to investigate the transfer direction of electrons. As shown in Figure S10, there was no major deviation in the C 1 s and N 1 s peak positions of CN before and after irradiation. However, in CNOFe-2, the C 1 s and N 1 s spectra were shifted to higher binding energies after irradiation, whereas the Fe 2 p spectra were shifted to lower binding

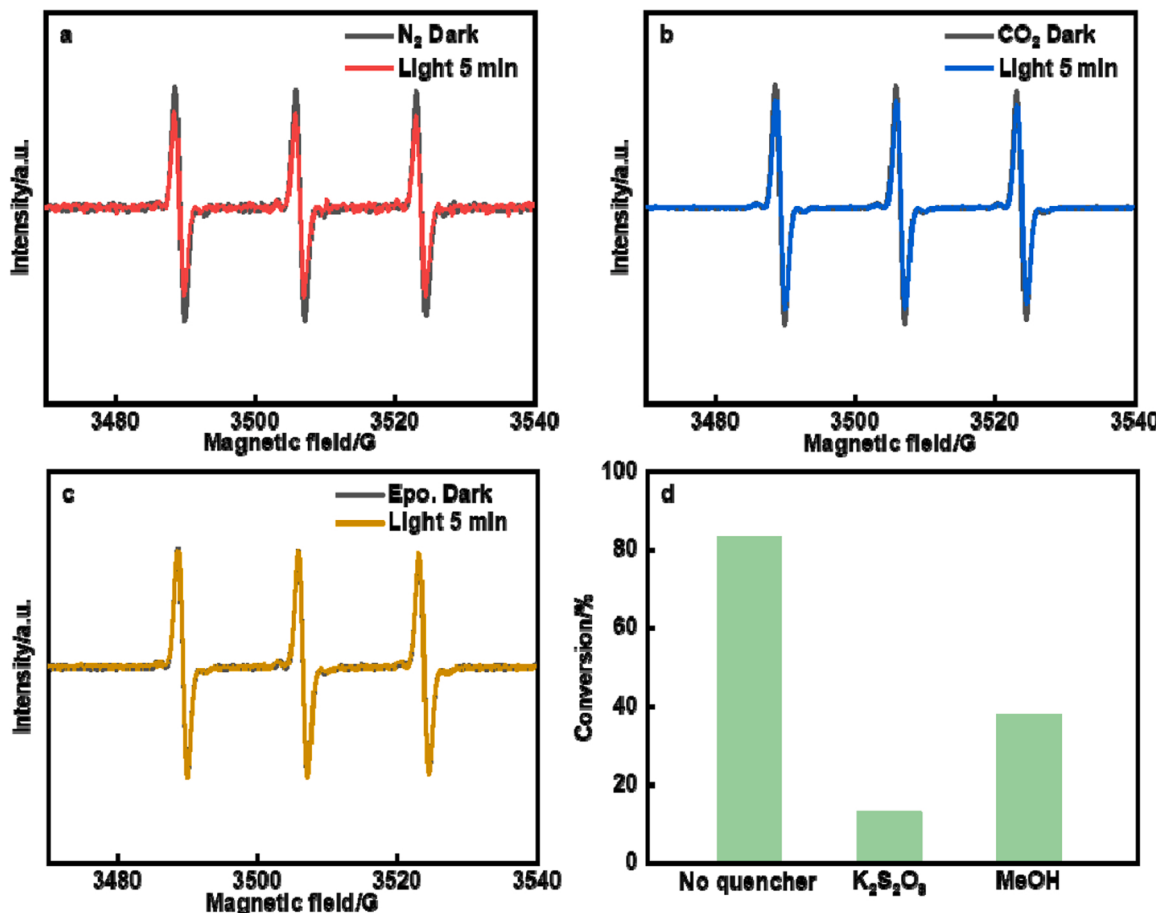


Fig. 6. EPR spectra of CNOFe-2 obtained under different test conditions: (a) N₂, (b) CO₂, and (c) CO₂ atmosphere with styrene oxide added; (d) photocatalytic CO₂ cycloaddition reaction performance of CNOFe-2 with the addition of different quenchers.

energies, suggesting that photogenerated electrons were transferred from O-g-C₃N₄ to FeO_x [40].

The proposed mechanism of this photocatalytic CO₂ cycloaddition reaction on FeO_x/O-g-C₃N₄ samples is schematically displayed in Fig. 7.

To begin, the activation of styrene oxide molecules occurs through

the interaction with Lewis acid Fe sites and the formation of hydrogen bonds between the -OH groups in the catalyst and the O atom in the epoxides [38]. Simultaneously, carbon dioxide undergoes activation facilitated by the abundant Lewis base-sites present on g-C₃N₄. Secondly, under irradiation, the -C≡N groups exhibit a tendency to attract

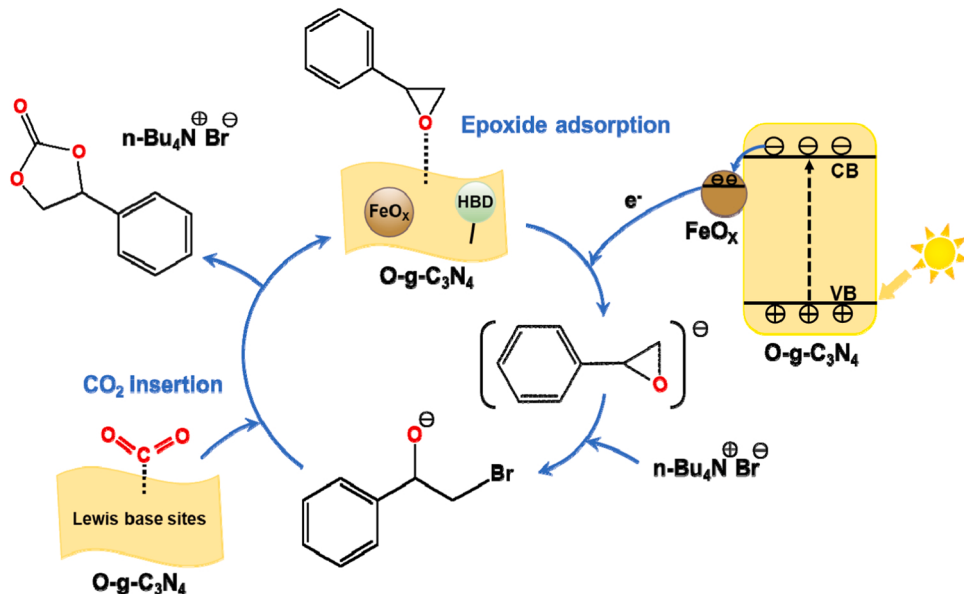


Fig. 7. Proposed mechanism-scheme for photocatalytic CO₂ cycloaddition reaction on FeO_x/O-g-C₃N₄.

photoelectrons, enhancing the efficient separation of charge carriers in O-g-C₃N₄ [41,42]. The photoelectrons on O-g-C₃N₄ swiftly transfer to FeO_x [23], where they involve in reactions with activated epoxides, leading to the formation of negatively charged styrene oxide intermediates. Concurrently, photogenerated holes play a role in the activation of epoxides, acting as Lewis acid-sites. Subsequently, the Br⁻ in TBAB initiates an attack on the less hindered C atom of styrene oxide, resulting in the formation of ring-opening intermediates. The subsequent steps involve styrene carbonate formation and TBAB regeneration, achieved through CO₂ insertion and intramolecular cyclization. This intricate process outlines the sequential steps involved in the catalytic mechanism.

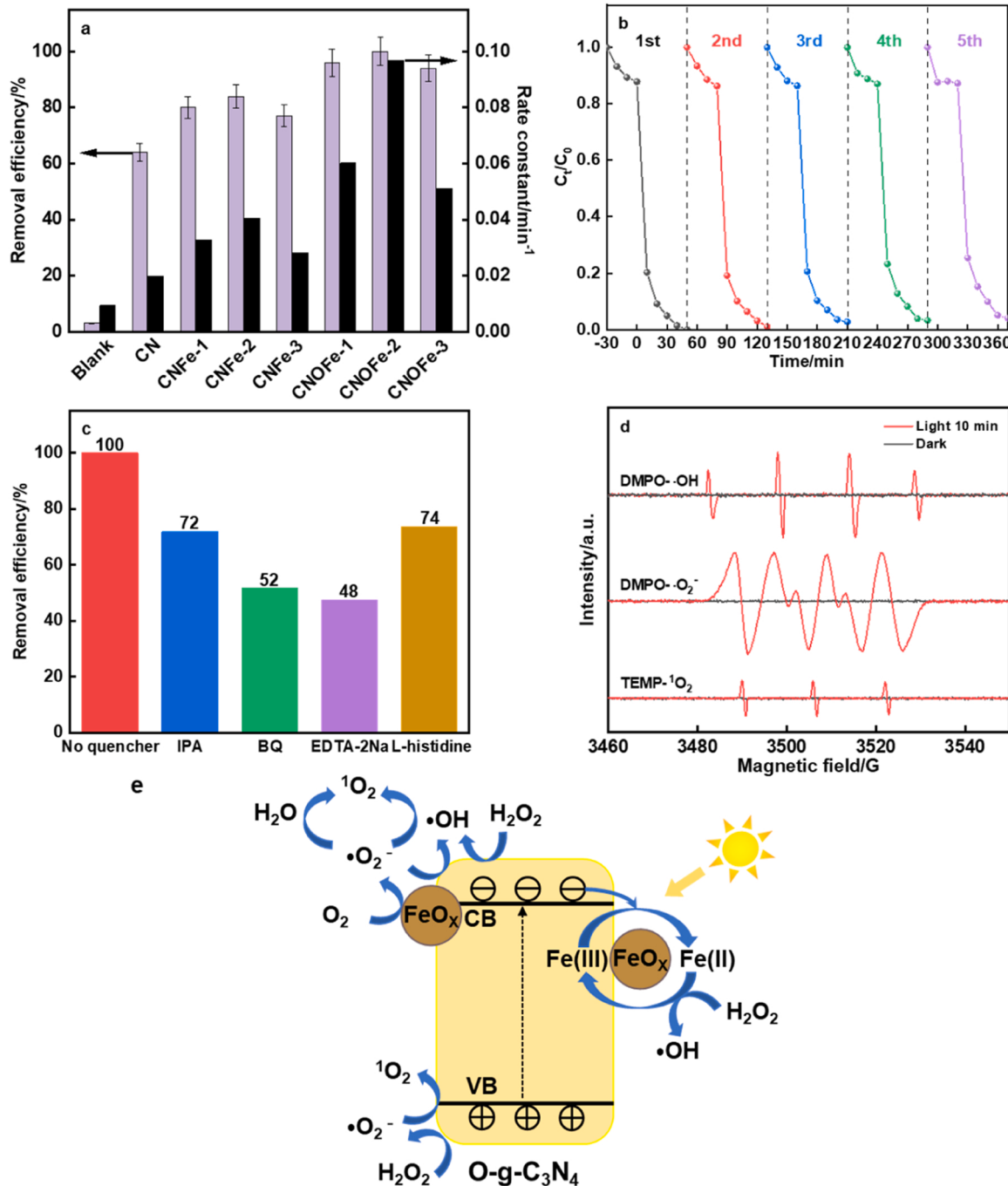


Fig. 8. The photo-Fenton TC degradation performance of: (a) all the samples after 50 min irradiation, (b) 5 consecutive runs of cyclic experiment on CNOFe-2, and (c) CNOFe-2 with different quenchers added; (d) EPR spectra of DMPO-O₂⁻, DMPO-OH, and TEMP-¹O₂ on CNOFe-2, and (e) plausible photo-Fenton TC degradation mechanism over FeO_x/O-g-C₃N₄.

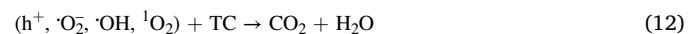
achieving complete TC degradation in 50 min. The rate constant of CNOFe-2 reached 0.0947 min^{-1} , which is 4.7 times faster than that of CN. CNOFe-2 demonstrated excellent performance stability, with a degradation rate difference of only 6% in 5 consecutive cyclic experiment (Fig. 8b). As listed in Table S3, this FeO_x/O-g-C₃N₄ photocatalyst has performance advantages over the currently reported photocatalytic Fenton systems.

To reveal the synergistic effect of the Fenton reaction and photocatalysis, control tests were performed on CNOFe-2 (Figure S11b). The removal rate of CNOFe-2 declined tremendously to 37% without illumination and 48% without H₂O₂ added, exhibiting the advantage of this photo-Fenton system. The effects of catalyst and H₂O₂ dosage on the photo-Fenton TC removal were studied. When the catalyst dosages of CNOFe-2 were changed to 10 and 50 mg, the TC removal rates within 50 min became 81% and 97%, respectively (Figure S11c). Although H₂O₂ dosage has little effect on the total removal rate within 50 min, the reaction rate changes significantly (Figure S11d). When using 100, 200, and 300 μL, the reaction rates of CNOFe-2 are 0.0559, 0.0947, and 0.083 respectively.

To uncover the process behind this photo-Fenton TC degradation over CNOFe-2, quenchers including IPA, BQ, EDTA-2Na, and L-histidine were added to eliminate ·OH, ·O₂⁻, h⁺, and ¹O₂ radicals, respectively. Fig. 8c reflects that all the above radicals are active species. IPA or histidine addition contribute to a slightly reduced TC removal rate, from 100% to 72% and 74%, respectively. However, the addition of BQ or EDTA-2Na results in a significantly decreased removal efficiency, from 100% to 52% or to 48%, respectively.

The radicals in the photo-Fenton system were further detected by EPR, as shown in Fig. 8d. Firstly, DMPO (3, 4-Dihydro-2, 2-Dimethyl-2 H-pyrrole1-oxide) is applied as spin labeling for ·OH radicals, where four typical peaks with 1:2:2:1 intensity ratio can be observed after 5 min irradiation [43]. The bandgaps of CN, CNFe-2 and CNOFe-2, exacted from the corresponding Tauc plots (Figure S12a), are 2.96, 2.94, and 2.70 eV, respectively. For a n-type semiconductor, the conduction band edge potential (E_{CB}) is 0.1 eV below flat band potential [44]. Based on the Mott-Schottky plots (Figure S12b-d) and Nernst equation ($E_{NHE} = E_{Ag/AgCl} + 0.1976$), the E_{CB} of CN, CNFe-2 and CNOFe-2 are estimated at -0.85, -1.01, and -1.15 eV, respectively. Combined with the bandgap data, the corresponding valence band edge potentials (E_{VB}) of CN, CNFe-2 and CNOFe-2 are calculated to be 2.11, 1.83, and 1.45 eV, respectively. Thus, the E_{VB} of CNFe-2 and CNOFe-2 are more negative than the potentials of OH⁻/OH (1.99 eV) and H₂O/OH (2.37 eV) [45]. Consequently, OH⁻ or H₂O cannot be oxidized by the photo-induced holes in CNOFe-2's VB to produce ·OH. The ·OH radicals in the system could result from the direct reaction of photoelectrons with H₂O₂ (Eq. (1)) and the Fenton process between Fe²⁺ and H₂O₂ (Eq. (2)). The Fe²⁺/Fe³⁺ cycle was completed by Eqs. (3)–(4) [46]. Secondly, 4 main characteristic peaks of DMPO-·O₂⁻ with 1:1:1:1 intensity ratio were also detected. The E_{CB} of CNFe-2 and CNOFe-2 were more negative than the potential of O₂/·O₂⁻ (-0.33 eV), with values of -1.22 and -1.53 eV, respectively. Thus, superoxide radical (·O₂⁻) could be formed through the reaction of ·OH with H₂O₂, O₂ with e⁻, or h⁺ with H₂O₂ (Eqs. (5)–(7)) [47]. The ionization of ·OOH could also produce ·O₂⁻ (Eq. (8)).

Besides, ¹O₂ is labeled by TEMP (2,2,6,6-tetramethyl-4-piperidone hydrochloride) and a triplet signal with relative intensities of 1:1:1 appeared. ¹O₂ could be produced when ·O₂⁻ reacts with h⁺, H₂O, or ·OH radicals (Eqs. (9)–(11)) [48]. As a result, ·O₂⁻ radicals and h⁺ play crucial role in this photo-Fenton reaction, while ·OH and ¹O₂ radicals simultaneously contribute to the complete degradation of TC (Eq. (12)).



Thus, Fig. 8e illustrates a plausible photo-Fenton TC degradation mechanism over FeO_x/O-g-C₃N₄ samples. Under illumination, the photoelectrons would migrate from O-g-C₃N₄ to amorphous FeO_x, where O₂ is reduced to ·O₂⁻. The -C≡N groups in O-g-C₃N₄ tend to attract photoelectrons, boosting superb charge carriers separation. The ·OH species are generated through the Fenton process on FeO_x and the photoelectrons participate in the Fe²⁺/Fe³⁺ cycling, facilitating H₂O₂ decomposition. The direct reactions of photo-induced electrons and holes with H₂O₂ would produce ·OH and ·O₂⁻, respectively. ·O₂⁻ could react with h⁺, H₂O, or ·OH radicals to produce ¹O₂, which also function as active substance for TC degradation. Superb photo-Fenton TC removal efficiency of FeO_x/O-g-C₃N₄ is achieved through the synergistic effect of photocatalysis and Fe²⁺-catalyzed H₂O₂ activation.

4. Conclusions

In this work, bifunctional FeO_x modified defective g-C₃N₄ were constructed using a straightforward one-step low-temperature calcination method. Charge carrier separation and transfer are facilitated by the photogenerated electrons-accepting nature of well-dispersed amorphous FeO_x species and -C≡N groups in O-g-C₃N₄. The FeO_x/O-g-C₃N₄ photocatalysts enriched with Lewis acid-base sites and hydrogen bond donor groups, exhibiting the highest 83% yield of styrene carbonate (23 mmol g⁻¹ h⁻¹) under mild condition. FeO_x incorporation also contributes to the excellent photo-Fenton performance of the photocatalysts in tetracycline degradation reaction, where h⁺, ·O₂⁻, ·OH, and ¹O₂ are proposed to be active species. This study offers a novel defect engineering strategy to construct efficient photocatalysts for CO₂ conversion and environmental remediation.

CRediT authorship contribution statement

Ruolin Cheng: Conceptualization, Formal analysis, Methodology, Writing – original draft. **Haoran Wang:** Methodology, Writing – review & editing. **Jing Ren:** Formal analysis, Methodology. **PANAGIOTIS TSIAKARAS:** Writing – review & editing, Conceptualization. **Huagen Liang:** Writing – review & editing, Supervision, Methodology, Conceptualization.

Declaration of Competing Interest

The authors declare that they have no known competing financial interests or personal relationships that could have appeared to influence the work reported in this paper.

Data availability

Data will be made available on request.

Acknowledgments

This work was financially supported by the Fundamental Research

Funds for the Central Universities (No. 2023QN1067), “Double Innovation” Doctor of Jiangsu Province, the National Natural Science Foundation of China (No. 21908242), and the Foundation of Science and Technology Project of Xuzhou City (No. KC22044). The authors express their gratitude to Theoretical and Computational Chemistry Team from Shiyanjia Lab (www.shyanjia.com) for providing invaluable assistance.

Appendix A. Supporting information

Supplementary data associated with this article can be found in the online version at [doi:10.1016/j.apcatb.2024.124024](https://doi.org/10.1016/j.apcatb.2024.124024).

References

- [1] C.C. Liu, X. Zhang, Y.L. Cheng, X.Q. Hao, P. Yang, NiS/Ni₃S₄ decorated double-layered hollow carbon spheres for efficient electrochemical hydrogen evolution reaction and supercapacitor, *Electrochimica Acta* 477 (2024) 143751, <https://doi.org/10.1016/j.electacta.2023.143751>.
- [2] X.S. Ji, B.G. Xu, H.Y. Zhang, X. Zhang, P. Yang, NiS₂ nanoparticles anchored on Co-carbon nanotubes for supercapacitor and overall water splitting, *J. Alloy Compd.* 968 (2023) 172192, <https://doi.org/10.1016/j.jallcom.2023.172192>.
- [3] J.X. Li, C.G. Yue, W.H. Ji, B.M. Feng, M.Y. Wang, X.B. Ma, Recent advances in cycloaddition of CO₂ with epoxides: halogen-free catalysis and mechanistic insights, *Front. Chem. Eng.* (2023), <https://doi.org/10.1007/s11705-023-2354-4>.
- [4] T. Yan, H. Liu, Z.X. Zeng, W.G. Pan, Recent progress of catalysts for synthesis of cyclic carbonates from CO₂ and epoxides, *J. CO₂ Util.* 68 (2023) 102355, <https://doi.org/10.1016/j.jcou.2022.102355>.
- [5] Y. Liu, S.J. Li, M. Pudukudy, L. Lin, H.G. Yang, M.R. Li, S.Y. Shan, T.D. Hu, Y.F. Zhi, Melamine-based nitrogen-heterocyclic polymer networks as efficient platforms for CO₂ adsorption and conversion, *Sep. Purif. Technol.* 331 (2024) 125645, <https://doi.org/10.1016/j.seppur.2023.125645>.
- [6] X. Zhang, P. Yang, g-C₃N₄ Nanosheet Nanoarchitectonics: H₂ Generation and CO₂ Reduction, *Chemnanomat* 9 (2023) e202300041, <https://doi.org/10.1002/cnma.202300041>.
- [7] T. Song, X. Zhang, C. Xie, P. Yang, N-doped carbon nanotubes enhanced charge transport between Ni nanoparticles and g-C₃N₄ nanosheets for photocatalytic H₂ generation and 4-nitrophenol removal, *Carbon* 210 (2023) 118052, <https://doi.org/10.1016/j.carbon.2023.118052>.
- [8] T. Song, X. Zhang, K. Matras-Postolek, P. Yang, N-doped carbon layer promoted charge separation/transfer in WP/g-C₃N₄ heterostructures for efficient H₂ evolution and 4-nitrophenol removal, *Carbon* 202 (2023) 378–388, <https://doi.org/10.1016/j.carbon.2022.11.008>.
- [9] X. Zhang, K.L. Zhu, C. Xie, P. Yang, Vertically implanting MoSe₂ nanosheets on superior thin C-doped g-C₃N₄ nanosheets towards interface-enhanced electrochemical activities, *Carbon* 220 (2024) 118884, <https://doi.org/10.1016/j.carbon.2024.118884>.
- [10] X. Zhang, P. Yang, Role of graphitic carbon in g-C₃N₄ nanoarchitectonics towards efficient photocatalytic reaction kinetics: A review, *Carbon* 216 (2024) 118584, <https://doi.org/10.1016/j.carbon.2023.118584>.
- [11] X. Zhang, P. Yang, H.S. Chen, S.P. Jiang, Carbon layer derived carrier transport in Co/g-C₃N₄ nanosheet junctions for efficient H₂O₂ production and NO removal, *Chem. Eng. J.* 479 (2024) 147609, <https://doi.org/10.1016/j.cej.2023.147609>.
- [12] X. Zhang, H.S. Chen, S.P. Jiang, P. Yang, W₁₈O₄₉/crystalline g-C₃N₄ layered heterostructures with full solar energy harvesting towards efficient H₂O₂ generation and NO, *Nano Energy* 120 (2024) 109160, <https://doi.org/10.1016/j.nanoen.2023.109160>.
- [13] N. El Messaoudi, Z. Cigeroglu, Z.M. Senol, M. Elhajam, L. Noureen, A comparative review of the adsorption and photocatalytic degradation of tetracycline in aquatic environment by g-C₃N₄-based materials, *J. Water Process Eng.* 55 (2023) 104150, <https://doi.org/10.1016/j.jwpe.2023.104150>.
- [14] D. Zhang, T. Xu, C. Li, W. Xu, J. Wang, J. Bai, Synthesis of carbon fibers support graphitic carbon nitride immobilize ZnBr₂ catalyst in the catalytic reaction between styrene oxide and CO₂, *J. CO₂ Util.* 34 (2019) 716–724, <https://doi.org/10.1016/j.jcou.2019.09.005>.
- [15] Y. Li, S. Weng, S. Wang, G. Zhang, F. Liu, M. Liu, Engineering the activity and stability of ZIF-8(Zn/Co)@g-C₃N₄ nanocomposites and their synergistic action in converting atmospheric CO₂ into cyclic carbonates, *J. Colloid Interface Sci.* 656 (2024) 24–34, <https://doi.org/10.1016/j.jcis.2023.11.085>.
- [16] Y. Gu, R. Ping, F. Liu, G. Zhang, M. Liu, J. Sun, Novel carbon nitride/metal oxide nanocomposites as efficient and robust catalysts for coupling of CO₂ and epoxides, *Ind. Eng. Chem. Res.* 60 (2021) 5723–5732, <https://doi.org/10.1016/acs.iecr.0c05966>.
- [17] W. Dai, M. Zou, J. Long, B. Li, S. Zhang, L. Yang, D. Wang, P. Mao, S. Luo, X. Luo, Nanoporous N-doped carbon/znO hybrid derived from zinc aspartate: An acid-base bifunctional catalyst for efficient fixation of carbon dioxide into cyclic carbonates, *Appl. Surf. Sci.* 540 (2021) 148311, <https://doi.org/10.1016/j.apsusc.2020.148311>.
- [18] H. Jiang, C. Zang, L. Guo, X. Gao, Carbon vacancies enriched carbon nitride nanotubes for Pd coordination environment optimization: Highly efficient photocatalytic hydrodechlorination and CO₂ cycloaddition, *Sci. Total Environ.* 838 (2022) 155920, <https://doi.org/10.1016/j.scitotenv.2022.155920>.
- [19] A. Kumar, S. Samanta, R. Srivastava, Graphitic carbon nitride modified with Zr-Thiamine complex for efficient photocatalytic CO₂ insertion to epoxide: Comparison with traditional thermal catalysis, *ACS Appl. Nano Mater.* 4 (2021) 6805–6820, <https://doi.org/10.1021/acsnano.1c00887>.
- [20] X. Zhang, K. Matras-Postolek, P. Yang, S.P. Jiang, Pt clusters in carbon network to enhance photocatalytic CO₂ and benzene conversion of WO_x/g-C₃N₄ nanosheets, *Carbon* 214 (2023) 118337, <https://doi.org/10.1016/j.carbon.2023.118337>.
- [21] V.W.H. Lau, I. Moudrakovski, T. Botari, S. Weinberger, M.B. Mesch, V. Duppel, J. Senker, V. Blum, B.V. Lotsch, Rational design of carbon nitride photocatalysts by identification of cyanamide defects as catalytically relevant sites, *Nat. Commun.* 7 (2016) 12165, <https://doi.org/10.1038/ncomms12165>.
- [22] D.S. Zhang, P.J. Ren, W.W. Liu, Y.R. Li, S. Salli, F.Y. Han, W. Qiao, Y. Liu, Y.Z. Fan, Y. Cui, Y.B. Shen, E. Richards, X.D. Wen, M.H. Rummeli, Y.W. Li, F. Besenbacher, H. Niemantsverdriet, T.B. Lim, R. Su, Photocatalytic abstraction of hydrogen atoms from water using hydroxylated graphitic carbon nitride for hydrogenative coupling reactions, *Angew. Chem. Int. Ed.* 61 (2022) e202204256, <https://doi.org/10.1002/anie.202204256>.
- [23] R.L. Cheng, L.X. Zhang, X.Q. Fan, M. Wang, M.L. Li, J.L. Shi, One-step construction of FeOx modified g-C₃N₄ for largely enhanced visible-light photocatalytic hydrogen evolution, *Carbon* 101 (2016) 62–70, <https://doi.org/10.1016/j.carbon.2016.01.070>.
- [24] X.Q. Tang, Y.D. Zhang, Z.W. Jiang, D.M. Wang, C.Z. Huang, Y.F. Li, Fe₃O₄ and metal organic framework MIL-101(Fe) composites catalyze luminol chemiluminescence for sensitively sensing hydrogen peroxide and glucose, *Talanta* 179 (2017) 43–50, <https://doi.org/10.1016/j.talanta.2017.10.049>.
- [25] M. Wang, Z. Shu, L.X. Zhang, X.Q. Fan, G.J. Tao, Y.X. Wang, L.S. Chen, M.Y. Wu, J. L. Shi, Amorphous Fe²⁺-rich FeOx loaded in mesoporous silica as a highly efficient heterogeneous Fenton catalyst, *Dalton Trans.* 43 (2014) 9234–9241, <https://doi.org/10.1039/c4dt00105b>.
- [26] R.L. Cheng, A.H. Wang, S.X. Sang, H.G. Liang, S.Q. Liu, P. Tsikararas, Photocatalytic CO₂ cycloaddition over highly efficient W₁₈O₄₉-based composites: An economic and ecofriendly choice, *Chem. Eng. J.* 466 (2023) 142982, <https://doi.org/10.1016/j.cej.2023.142982>.
- [27] X. Zhang, P.J. Ma, C. Wang, L.Y. Gan, X.J. Chen, P. Zhang, Y. Wang, H. Li, L. H. Wang, X.Y. Zhou, K. Zheng, Unraveling the dual defect sites in graphite carbon nitride for ultra-high photocatalytic H₂O₂ evolution, *Energ. Environ. Sci.* 15 (2022) 830–842, <https://doi.org/10.1039/d1ee02369a>.
- [28] R.L. Cheng, X.X. Jin, X.Q. Fan, M. Wang, J.J. Tian, L.X. Zhang, J.L. Shi, Incorporation of N-Doped Reduced Graphene Oxide into Pyridine-Copolymerized g-C₃N₄ for Greatly Enhanced H₂ Photocatalytic Evolution, *Acta Phys. -Chim. Sin.* 33 (2017) 1436–1445, <https://doi.org/10.3866/Pku.Whxb201704076>.
- [29] J.W. Fu, B.C. Zhu, C.J. Jiang, B. Cheng, W. You, J.G. Yu, Hierarchical porous O-doped g-C₃N₄ with enhanced photocatalytic CO₂ reduction activity, *Small* 13 (2017) 1603938, <https://doi.org/10.1002/smll.201603938>.
- [30] Z.H. Li, Y.F. Chen, X.Y. Chen, L. Li, S. Kuang, Y.X. Guo, Y.N. Wang, J. Gao, Artificial visible light-induced H₂O₂ production using polymeric K/O-doped carbon nitride as a catalyst, *Appl. Surf. Sci.* 609 (2023) 155432, <https://doi.org/10.1016/j.apusc.2022.155432>.
- [31] Z.J. Zhao, J.J. Wu, Y.Z. Zheng, N. Li, X.T. Li, X. Tao, Ni₃C-Decorated MAPbI₃ as Visible-Light Photocatalyst for H₂ Evolution from HI Splitting, *ACS Catal.* 9 (2019) 8144–8152, <https://doi.org/10.1021/acscatal.9b01605>.
- [32] G. Zhai, Y. Liu, L. Lei, J. Wang, Z. Wang, Z. Zheng, P. Wang, H. Cheng, Y. Dai, B. Huang, Light-Promoted CO₂ Conversion from Epoxides to Cyclic Carbonates at Ambient Conditions over a Bi-Based Metal-Organic Framework, *ACS Catal.* 11 (2021) 1988–1994, <https://doi.org/10.1021/acscatal.0c05145>.
- [33] G.Y. Zhai, Y.Y. Liu, Y.Y. Mao, H.G. Zhang, L.T. Lin, Y.J. Li, Z.Y. Wang, H.F. Cheng, P. Wang, Z.K. Zheng, Y. Dai, B.B. Huang, Improved photocatalytic CO₂ and epoxides cycloaddition via the synergistic effect of Lewis acidity and charge separation over Zn modified UiO-bpydc, *Appl. Catal. B* 301 (2022) 120793, <https://doi.org/10.1016/j.apcatb.2021.120793>.
- [34] Y.Z. He, M.S. Xu, J.H. Xia, C.H. Zhang, X.T. Song, X.F. Zhao, M. Fu, S.Q. Li, X. Y. Liu, Effect of exposed active sites of semi-amorphous Fe-BTC on photocatalytic CO₂ cycloaddition reaction under ambient conditions, *Mol. Catal.* 542 (2023) 113134, <https://doi.org/10.1016/j.mcat.2023.113134>.
- [35] X.Q. Gong, Y.J. Zhang, Y.Y. Xu, G.Y. Zhai, X.L. Liu, X.L. Bao, Z.Y. Wang, Y.Y. Liu, P. Wang, H.F. Cheng, Y.C. Fan, Y. Dai, Z.K. Zheng, B.B. Huang, Synergistic effect between CO₂ chemisorption using amino-modified carbon nitride and epoxide activation by high-energy electrons for plasmon-assisted synthesis of cyclic carbonates, *ACS Appl. Mater. Interf.* 14 (2022) 51029–51040, <https://doi.org/10.1021/acsmami.2c16382>.
- [36] C.L. Tan, M.Y. Qi, Z.R. Tang, Y.J. Xu, Isolated Single-Atom Cobalt in the ZnIn₂S₄ Monolayer with Exposed Zn Sites for CO₂ Photofixation, *ACS Catal.* 13 (2023) 8317–8329, <https://doi.org/10.1021/acscatal.3c00992>.
- [37] A. Khalid, Z. Razzaq, P. Ahmad, B.S. Al-Anzi, F. Rehman, S. Muhammad, M. U. Khanda, G. Albasheer, N. Alsultani, I. Liaqat, D. Hayat, Visible-light promoted chemical fixation of carbon dioxide with epoxide into cyclic carbonates over S-scheme CdS-CeO₂ photocatalyst, *Mat. Sci. Semicon. Proc.* 165 (2023) 107649, <https://doi.org/10.1016/j.mssp.2023.107649>.
- [38] P. Qin, C. Zhang, Y.Y. Guo, D.L. Zhang, Q. Liu, Y.D. Li, H.B. Song, Z.G. Lv, Hydroxyl and amino dual-functionalized core-shell molecular sieves featuring hydrogen bond donor groups for efficient CO₂ cycloaddition, *J. Colloid Interface Sci.* 656 (2024) 68–79, <https://doi.org/10.1016/j.jcis.2023.11.088>.
- [39] J. Yang, X.Q. He, J. Dai, R. Tian, D.S. Yuan, Photo-assisted enhancement performance for rapid detoxification of chemical warfare agent simulants over versatile ZnIn₂S₄/UiO-66-NH₂ nanocomposite catalysts, *J. Hazard Mater.* 417 (2021) 126056, <https://doi.org/10.1016/j.jhazmat.2021.126056>.

- [40] Y.J. Wang, M.M. Liu, F. Fan, G. Li, J.X. Duan, Y.M. Li, G.Y. Jiang, W.Q. Yao, Enhanced full-spectrum photocatalytic activity of 3D carbon-coated C₃N₄ nanowires via giant interfacial electric field, *Appl. Catal. B* 318 (2022) 121829, <https://doi.org/10.1016/j.apcatb.2022.121829>.
- [41] B.B. Zhao, D.D. Gao, Y.P. Liu, J.J. Fan, H.G. Yu, Cyano group-enriched crystalline graphitic carbon nitride photocatalyst: Ethyl acetate-induced improved ordered structure and efficient hydrogen-evolution activity, *J. Colloid Interface Sci.* 608 (2022) 1268–1277, <https://doi.org/10.1016/j.jcis.2021.10.108>.
- [42] J. Wang, H. Zhao, B.C. Zhu, S. Larter, S.W. Cao, J.G. Yu, M.G. Kibria, J.G. Hu, Solar-driven glucose isomerization into fructose via transient Lewis acid-base active sites, *ACS Catal.* 11 (2021) 12170–12178, <https://doi.org/10.1021/acscatal.1c03252>.
- [43] Y. Zhang, L. Wang, H. Huang, C. Hu, X. Zhang, C. Wang, Y. Zhang, Water flow induced piezoelectric polarization and sulfur vacancy boosting photocatalytic hydrogen peroxide evolution of cadmium sulfide nanorods, *Appl. Catal. B* 331 (2023) 122714, <https://doi.org/10.1016/j.apcatb.2023.122714>.
- [44] L.L. Liu, F. Chen, J.H. Wu, M.K. Ke, C. Cui, J.J. Chen, H.Q. Yu, Edge electronic vacancy on ultrathin carbon nitride nanosheets anchoring O₂ to boost H₂O₂ photoproduction, *Appl. Catal. B* 302 (2022) 120845, <https://doi.org/10.1016/j.apcatb.2021.120845>.
- [45] X. Zhang, B. Ren, X. Li, B.M. Liu, S.W. Wang, P. Yu, Y.H. Xu, G.Q. Jiang, High-efficiency removal of tetracycline by carbon-bridge-doped g-C₃N₄/Fe₃O₄ magnetic heterogeneous catalyst through photo-Fenton process, *J. Hazard Mater.* 418 (2021) 126333, <https://doi.org/10.1016/j.jhazmat.2021.126333>.
- [46] C.Y. Hu, J.K. He, J.J. Liang, T. Lin, Q.L. Liu, Heterogeneous photo-Fenton catalyst α -Fe₂O₃@g-C₃N₄@NH₂-MIL-101(Fe) with dual Z-Scheme heterojunction for degradation of tetracycline, *Environ. Res.* 231 (2023) 116313, <https://doi.org/10.1016/j.envres.2023.116313>.
- [47] X.F. Li, X.L. Shen, Y.L. Qiu, Z.L. Zhu, H. Zhang, D.Q. Yin, Fe₃O₄ quantum dots mediated P-g-C₃N₄/BiOI as an efficient and recyclable Z-scheme photo-Fenton catalyst for tetracycline degradation and bacterial inactivation, *J. Hazard Mater.* 456 (2023) 131677, <https://doi.org/10.1016/j.jhazmat.2023.131677>.
- [48] C. Shao, J. Zhang, Z.Y. Wang, L.H. Zhang, B. Wang, J.L. Ren, X.D. Zhang, W.H. He, Photo-Fenton degradation of tetracycline on nitrogen vacancy and potassium-doped Z-scheme FeOCl/NvCN heterojunction with low H₂O₂ consumption: Activity and mechanism, *J. Alloy Compd.* 970 (2024) 172532, <https://doi.org/10.1016/j.jallcom.2023.172532>.